JGR Solid Earth

RESEARCH ARTICLE
10.1029/2020JB019762

Creep Along the Central San Andreas Fault From Surface Fractures, Topographic Differencing, and InSAR

Chelsea Scott[1], **Michael Bunds**[2], **Manoochehr Shirzaei**[3], **and Nathan Toke**[2]

[1]School of Earth and Space Exploration, Arizona State University, Tempe, AZ, USA, [2]Department of Earth Science, Utah Valley University, Orem, UT, USA, [3]Department of Geosciences, Virginia Tech, Blacksburg, VA, USA

Key Points:
- We measure tectonic creep along the central San Andreas Fault from surface fractures, topographic differencing and InSAR
- Light detection and ranging (lidar) and structure-from-motion topographic differencing capture deformation along and adjacent to the fault
- The majority of fault zone creep over a 1-km aperture is localized to less than 5-m

Supporting Information:
- Supporting Information S1
- Table S1

Correspondence to:
C. Scott,
cpscott1@asu.edu

Citation:
Scott, C., Bunds, M., Shirzaei, M., & Toke, N. (2020). Creep along the Central San Andreas Fault from surface fractures, topographic differencing, and InSAR. *Journal of Geophysical Research: Solid Earth*, *125*, e2020JB019762. https://doi.org/10.1029/2020JB019762

Received 11 MAR 2020
Accepted 4 OCT 2020
Accepted article online 7 OCT 2020

Abstract Imaging tectonic creep along active faults is critical for measuring strain accumulation and ultimately understanding the physical processes that guide creep and the potential for seismicity. We image tectonic deformation along the central creeping section of the San Andreas Fault at the Dry Lake Valley paleoseismic site (36.468°N, 121.055°W) using three data sets with varying spatial and temporal scales: (1) an Interferometric Synthetic Aperture Radar (InSAR) velocity field with an ~100-km footprint produced from Sentinel-1 satellite imagery, (2) light detection and ranging (lidar) and structure-from-motion 3-D topographic differencing that resolves a decade of deformation over a 1-km aperture, and (3) surface fractures that formed over the 3- to 4-m wide fault zone during a drought from late 2012 to 2014. The InSAR velocity map shows that shallow deformation is localized to the San Andreas Fault. We demonstrate a novel approach for differencing airborne lidar and structure-from-motion topography that facilitates resolving deformation along and adjacent to the San Andreas Fault. The 40-m resolution topographic differencing resolves a 2.5 ± 0.2 cm/yr slip rate localized to the fault. The opening-mode fractures accommodate $2.2^{+0.8}_{-0.6}$ cm/yr of fault slip. A 90% ± 30% of the 1-km aperture deformation is accommodated over the several meter-wide surface trace of the San Andreas Fault. The extension direction inferred from the opening-mode fractures and topographic differencing is 40°–48° from the local trend of the San Andreas Fault. The localization of deformation likely reflects the well-oriented and mature fault.

Plain Language Summary Typically, damaging earthquakes occur along faults as sudden movement following decades to millennia with very little to no fault motion. Creeping faults behave differently, slipping slowly and relatively continuously. While it may be easy to overlook the hazard they pose, moderate-magnitude earthquakes occur along creeping faults. Slip rates of several centimeters per year accumulate over time and can cause serious infrastructure damage to communities built along faults. We measure fault motion along the central portion of the creeping San Andreas Fault at a site located between Los Angeles and San Francisco. We constrain deformation at a variety of spatial scales including (1) movement over tens of kilometers from satellite radar imagery, (2) deformation within a 1-km aperture from light detection and ranging (lidar) and structure-from-motion topographic differencing, and (3) along the meter-scale width of the fault's trace from surface cracks. Integrating these data sets provides a new opportunity to image the 3-D fault zone structure, constrain fault slip rates, and analyze the strain budget. The data sets show that most if not all of the 2.5 cm/yr creep rate is localized to the 3- to 4-m wide fault at the Earth's surface. We attribute the high localization of deformation to the fault being mature and well-aligned for strike-slip movement.

1. Introduction

Recent advances in geodetic imaging of coseismic deformation have facilitated an increased understanding of the frictional behavior of the upper crust, on- and off-fault deformation, and seismic hazard (e.g., Barnhart et al., 2019; Brooks et al., 2017; Milliner et al., 2016; Nissen et al., 2014; Vallage et al., 2015; Wedmore et al., 2019). Topographic differencing techniques have been applied to resolve deformation along and adjacent to faults that have ruptured the surface (e.g., Howell et al., 2020; Scott et al., 2018, 2019), leading to constraints on shallow fault structure. The creeping portions of the San Andreas Fault, California, illustrate a range of behaviors including distributed deformation along geometric fault bends (e.g., DeLong et al., 2010; Lindsey et al., 2014), the presence of moderate magnitude (~M_w5–6.5) earthquakes (Bakun, 1999; Burgmann et al., 2000; Oppenheimer et al., 2010; Toppozada et al., 2002), and large earthquakes on adjacent locked segments that may be modulated by creep events (e.g., Arrowsmith et al., 1997; Khoshmanesh & Shirzaei, 2018b;

Murray & Langbein, 2006; Sieh, 1978). Along the central San Andreas Fault, displacement rates increase with distance from the fault (e.g., Titus et al., 2006). Such displacement gradients are either due to locked fault patches that accumulate strain that may later be released seismically (Johnson, 2013; Jolivet et al., 2015; Khoshmanesh & Shirzaei, 2018a; Tong et al., 2015) or may reflect slip partitioning along secondary structures (Johnson et al., 2018; Langenheim et al., 2013; Titus et al., 2007). Existing deformation rates measured with creep meters, alignment arrays, differential Global Navigation Satellite System (GNSS) (dGNSS), and Interferometric Synthetic Aperture Radar (SAR) (InSAR) are not spatially dense and/or lack sensitivity to the 3-D deformation field. Closing this gap in observations will facilitate a better understanding of the shallow fault zone (Chen & Bürgmann, 2017; Harris, 2017; Toke & Arrowsmith, 2006).

We present spatially dense deformation measurements at the Dry Lake Valley paleoseismic site (Toke & Arrowsmith, 2015; 36.468°N, 121.055°W) along the central San Andreas Fault. These observations are critical for constraining deformation within the fault zone. Shallow fault slip produces a sharp displacement gradient across the fault. However, a broader cross-fault gradient reflects shallow variations in fault slip, secondary fault activity, or distributed deformation. To determine how deformation is accommodated at Dry Lake Valley, we make observations at three spatial scales: At the largest scale, we use InSAR to measure displacements over an ~100-km footprint. We develop novel topographic differencing techniques to measure 3-D deformation from airborne light detection and ranging (lidar) and small uncrewed aerial system (sUAS)-derived topography at a 1-km aperture around the fault. This data set fills the gap between near-field analyses from alignment arrays, creep meters, and paleoseismology and far-field InSAR and GNSS observations. At the smallest scale, we assess the slip recorded in the surface cracking of soils during the 2012–2014 drought in California (Swain et al., 2014) along a 30 m-long stretch of the Dry Lake Valley site where the fault is straight and optimally aligned for right-lateral strike movement.

This paper is organized as follows: In section 2, we provide an overview of the Central San Andreas Fault and the Dry Lake Valley site. In section 3, we discuss constraints on deformation from InSAR, 3-D topographic differencing, and surface fracturing. For differencing, we emphasize approaches to decrease displacement and the fault slip rate error. We discuss fracture geometry, opening, and timing relative to a drought. We compare fault deformation observed from the three data sets and discuss the localization of deformation in terms of fault maturity and geometric complexity in section 4.

2. Central San Andreas Fault and Dry Lake Valley

The San Andreas Fault forms the primary boundary between the North American and Pacific plates, whose relative velocity is 45 mm/yr (DeMets et al., 1994). As shown in Figure 1, the central creeping section of the San Andreas Fault extends 140 km, from Parkfield North to San Juan Bautista and is bounded by locked fault segments that hosted the 1857 M7.9 Fort Tejon and 1906 M7.9 San Francisco earthquakes. The largest fault creep rate of over 30 mm/yr occurs at Bitterwater and was measured with an alignment array (Burford & Harsh, 1980). At Dry Lake Valley, Burford and Harsh's (1980) alignment array from 1967 to 1974 resolves a 21.9 $\pm$ 0.4 mm/yr creep rate. The San Andreas Fault overlaps with the Calaveras fault that creeps at 7–9 mm/yr at a location 10–15 km northeast of Dry Lake Valley (Lisowski & Prescott, 1981).

Dry Lake Valley is 11 km northwest of Bitterwater and a few kilometers from Pinnacles National Park. It was the focus of paleoseismic studies by Toke and Arrowsmith (2015). Immediately southeast of Dry Lake Valley, the San Andreas Fault crosses rugged terrain, as shown in Figure 2. It cuts along a trough on the southwestern side of a 50- to 150-m high ridge with three beheaded drainages with westward flow. The fault enters Dry Lake Valley where the ridge ends and cuts across low-relief alluvial fan surfaces emanating from the western slopes of Buck Ridge. The fault trace bounds an ~150 m-long sag pond produced by an ~50 m-wide right fault step. For 2-km to the northwest, the fault trace is straight and has a 2- to 7-m-tall fault scarp with the northeast-side up. Dry Lake Valley is bordered and likely underlain by Pliocene to Quaternary marine and non-marine sediments (Jennings & Strand, 1958).

In 2012 and 2013, Toke and Arrowsmith (2015) documented an ~5,000-yr record of sedimentation and deformation at Dry Lake Valley from nine fault trenches (Figure 2). The trenches revealed pervasive deformation fabrics including highly fractured stiff soils associated with a localized fault zone below the surface trace. The buried fractures were filled with fine sediments. On average, they were oriented 42° to the local fault trend,

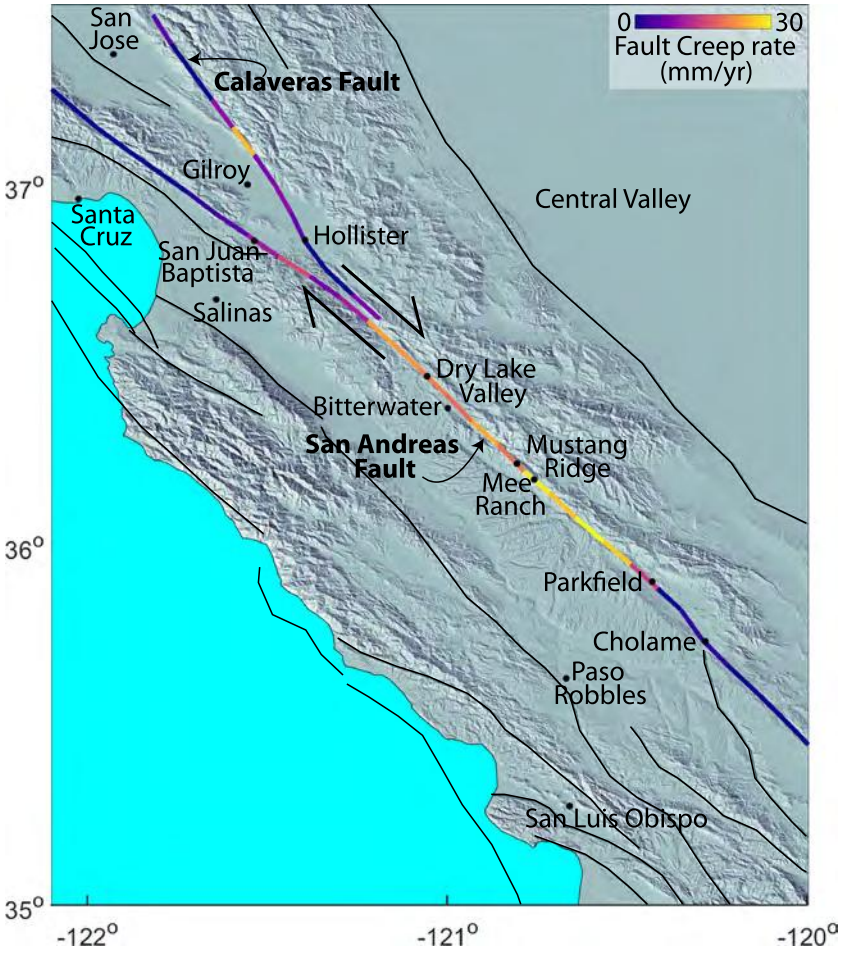

Figure 1. Overview map of the Central San Andreas Fault and other faults in Central California. Fault creep rates along the San Andreas and Calaveras faults are from Tong et al. (2013). Black lines are faults from the USGS/CGS quaternary faults and folds database (https://www.usgs.gov/natural-hazards/earthquake-hazards/faults).

had meter scale lengths ranging from ~0.5-m to larger than the ~2-m trench width, and had opening apertures ranging from 0–8 cm with a 2-cm average.

3. Methods

3.1. Far-Field Deformation: InSAR Processing

To detect surface deformation along the San Andreas Fault over an ~100-km footprint, we applied a multi-temporal SAR interferometric analysis (Shirzaei, 2013) to a set of 101 SAR images acquired by the Sentinel-1A/B C-band satellites from November 2015 to January 2020 in descending Frame 472 and Path 42 (heading ~193.1° and incidence ~33.9°). We co-registered the single look complex (SLC) images to a reference image using a standard matching algorithm, a digital elevation model (DEM), 3-D precise orbital parameters, and amplitude images (Sansosti et al., 2006). The precise orbits yielded a 5-cm 1σ 3-D position accuracy (ESA, 2020), which eliminates the need for any additional correction to reduce residual orbital errors in differential interferograms. Next, we applied an enhanced spectral diversity (ESD) approach (Shirzaei et al., 2017; Yague-Martinez et al., 2016). Using this data set, we generated 404 high-quality interferograms (Figure S2, supporting information). We performed multi-looking by a factor of 32 and 6 in range and azimuth, respectively, resulting in an ~75 × 75 m ground pixel resolution. We removed the topographic phase (Franceschetti & Lanari, 1999) and performed the flat earth correction using the Shuttle Radar Topography Mission DEM (Farr et al., 2007) and precise satellite orbital information.

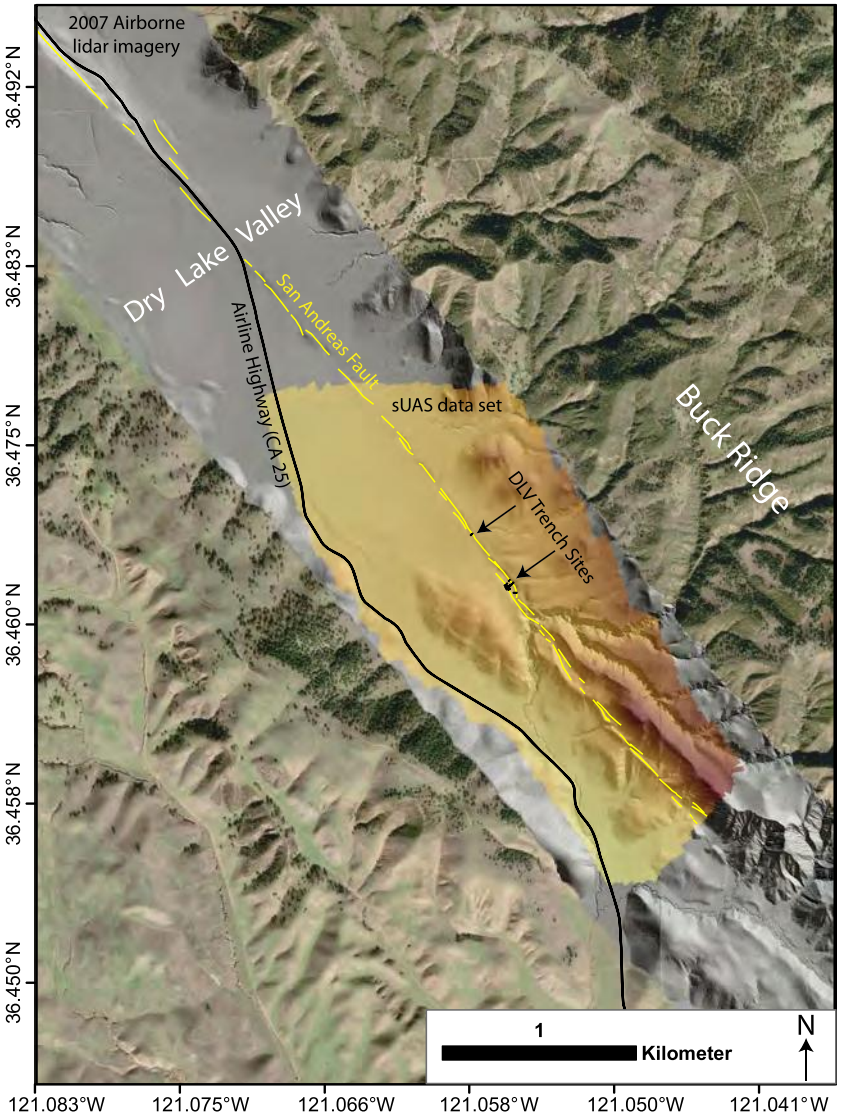

Figure 2. Topographic hillshade from the 2007 EarthScope airborne lidar and a base map at Dry Lake Valley along the Central San Andreas Fault. Map shows the 2017 sUAS coverage (Bunds et al., 2020), the trench site (Toke & Arrowsmith, 2015), and Buck Ridge.

To identify elite pixels with lower noise, we calculated the time-series of the complex interferometric phase noise for each pixel using a wavelet multiresolution analysis (Shirzaei, 2013). Next, we identified elite pixels by applying a hypothesis test at a 95% confidence level using a chi-square probability density function (Shirzaei, 2013). To obtain absolute values of the phase changes for elite pixels, we conducted sparse phase unwrapping (Constantini & Rosen, 1999) using a minimum cost flow (MCF) algorithm (Costantini, 1998). To correct for the spatially uncorrelated atmospheric delay, we applied a 2-D wavelet multiresolution filter using Coiflet base functions in one level of decomposition (Shirzaei & Bürgmann, 2012). To solve for the surface deformation time series, we applied re-weighted least squares (Shirzaei & Bürgmann, 2013). In each iteration, the observation weight matrix is updated based on residuals from the previous iteration (Shirzaei, 2013). The iteration stopped when either the improvement in the subsequent solution is less than 10^{-10} or the iteration number exceeds 100. We further reduced residual atmospheric errors by applying a high pass filter based on a 1-D continuous wavelet using a derivative of the Gaussian continuous wavelet base function. The number of wavelets scales so that after the wavelet decomposition, the extracted component of the maximum period is ~300 days (Torrence & Compo, 1998). We obtained the denoised time series by adaptive filtering of the wavelet coefficients at each level of the decomposition (Gao et al., 2010) and then

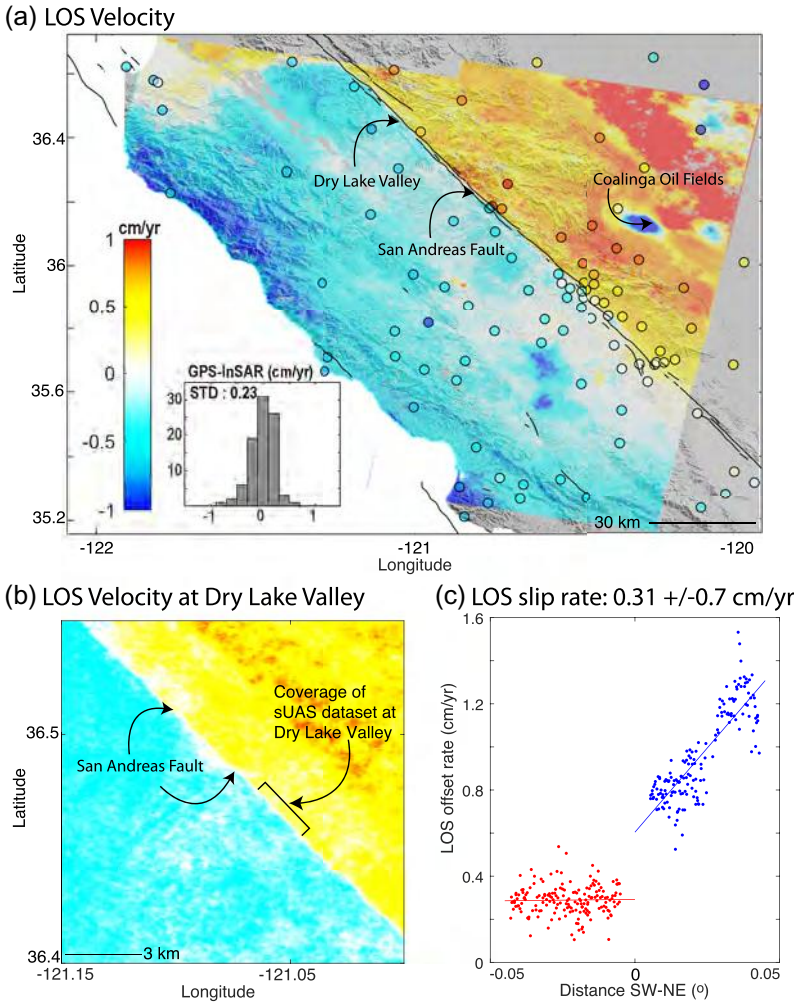

Figure 3. (a) Sentinel-1 rate map along the San Andreas Fault from November 2015 to December 2019 (heading angle ~193.1°, center-scene incidence angle ~33.9°). Blue and red colors indicate movement away from and towards satellite, respectively. Circles denote GNSS stations, color-coded with 3-D displacement rates projected to the satellite's line of sight. Black lines are faults from the USGS/CGS quaternary faults and folds database (https://www.usgs.gov/natural-hazards/earthquake-hazards/faults). Inset: Histogram of the difference between InSAR and GNSS line-of-sight velocities with a standard deviation (STD) of 0.23 cm/yr. (b) Zoom to the Sentinel-1 line-of-sight rate map near Dry Lake Valley with the same color scale as (a). (c) Line-of-sight fault slip rate calculation at Dry Lake Valley.

reconstructing the signal following the inverse wavelet transform. The long-term line-of-sight (LOS) displacement rates are the slope to the best-fitting line of the surface deformation time series.

Figure 3a shows the spatial distribution of the LOS velocity field along the San Andreas Fault. The cooler colors indicate movement away from the satellite, while warmer ones indicate motion towards the satellite. Circles present GNSS stations, color-coded to the 3-D displacement rate projected to the SAR satellite LOS (Hanssen, 2001). The projected GNSS and InSAR rates differ by a standard deviation of 0.23 cm/yr, showing good agreement. Assuming GNSS measurements as ground-truth, we consider the 0.23 cm/yr as the InSAR velocity map accuracy for studying near-field observations.

Solving for the right-lateral fault slip rate from the single LOS would require knowing or assuming the sense of motion. While the topographic differencing shows only negligible vertical and fault-perpendicular rates (see below), we only calculated the displacement in the SAR LOS as this avoids possible contamination in the right-lateral slip rate from vertical and fault-perpendicular ground displacement. We calculated the LOS fault slip rate using the displacement-projection method which we also apply to the topographic differencing displacements. For InSAR, we selected rates within ~0.05° of the fault along fault-perpendicular

500-m wide transects. We solved for the best-fit line along each side of the fault, and the slip rate is the difference between the lines projected to the fault. The transect in Figure 3c is at the center of the Dry Lake Valley site, and the uncertainty represents the standard deviation of all transects at Dry Lake Valley.

3.2. Intermediate-Field Deformation: Point Cloud Generation and Topographic Differencing

3.2.1. Point Clouds for Topographic Differencing

While lidar is commonly used to acquire submeter-scale digital topography, the high costs are often prohibitive for research groups interested in acquiring multitemporal data over modest-sized areas. Structure from motion (SfM) is an alternative approach and uses concepts from stereo-photogrammetry (e.g., Johnson et al., 2014) to build the geometry by applying triangulation to optical images. Advances in feature recognition with the scale-invariant feature transform algorithm (Lowe, 2004; Snavely et al., 2008) allow for highly variable camera perspective and angle. Texture in SfM point clouds is recorded in red-green-blue color, and the resulting point cloud is typically only sensitive to the top of vegetation. In contrast, lidar measures intensity and samples through most vegetation.

Bunds et al. (2020) generated a point cloud from imagery collected by a Sensefly eBee Plus sUAS on 27 and 28 October 2017 that flew at ~120 m above ground level. The 3,533 sUAS optical photographs had an average ground pixel size of ~2.8 cm. The eBee Plus, a fixed-wing sUAS, incorporated a dual-frequency GNSS that recorded positions at 1 Hz and time-stamped each photograph. Bunds et al. (2020) calculated post-processed kinematic (PPK) eBee GNSS positions using a local reference station that recorded ~13 h of 1-Hz position measurements from a Septentrio PolaRx5 receiver with a Trimble Zephyr Geodetic II antenna. The reference station position was calculated using the National Geodetic Survey (NGS) Online Positioning User Service, and the position was transformed to ITRF 2000 epoch 2007.2 to match the EarthScope lidar (EarthScope, 2008; Prentice et al., 2009) using the NGS Horizontal Time-Dependent Positioning calculator (Pearson & Snay, 2013; Snay, 1999, 2003).

The point cloud was produced using a standard SfM workflow in Agisoft Metashape. Processing steps included the following: Generate tie points (sparse point cloud) using the "Highest" setting, apply dGNSS camera positions for georeferencing, and iteratively perform bundle adjustments after removing tie points with large uncertainty. The dense point cloud created on the "High" setting has 1.2×10^9 points over 2.7 km^2. The high setting downsampled the photographs by a factor of two, creating one point per ground area covered by four photograph pixels. The point cloud was initially 10.2 cm above 30 independently measured checkpoints and therefore was translated downward. The horizontal and vertical root mean square errors are 2.1 and 3.8 cm, respectively, relative to checkpoints.

The 2007 airborne lidar data set (EarthScope, 2008) that we use for differencing has a 9.4 pts/m^2 point density and was collected with airplane flight lines parallel to the San Andreas Fault. Alignment errors (Shan et al., 2007) between overlapping flight lines create corduroy patterns in topographic hillshades and linear artifacts in the displacement fields, as described below.

3.2.2. 3-D Differencing

To calculate 3-D displacements between the 2007 EarthScope lidar and the 2017 SfM point clouds, we use a windowed implementation of the point-to-plane iterative closest point (ICP) algorithm (Besl & McKay, 1992; Chen & Medioni, 1992; Nissen et al., 2012; Scott et al., 2018). This approach finds the best rotation and translation to align decameter-scale windows of the topography data sets and has been applied to terrestrial laser scanning (TLS), airborne laser scanning, airborne aerial imagery, and stereo-satellite-derived topography (e.g., Barnhart et al., 2019; Howell et al., 2020; Nissen et al., 2014; Scott et al., 2018; Wedmore et al., 2019). We use the LibICP algorithm developed by Geiger et al. (2012). The ideal window size (i.e., displacement resolution) is a trade-off between a small window that is less likely to violate the rigid body assumption and a larger window size that typically has more features to produce a better alignment (Nissen et al., 2012). We describe our differencing result as a "rate" representative of the average rate over the decade between the data set acquisitions.

Our analysis represents hybrid differencing: The 2007 airborne lidar samples both vegetation and the bare earth while the 2017 SfM-derived data are primarily sensitive to surface features. Because the data sets do not typically view identical surfaces, producing a precise alignment is challenging. Apparent vertical deformation may reflect vegetation change. The sUAS has a point density that is ~45 times higher than the lidar data.

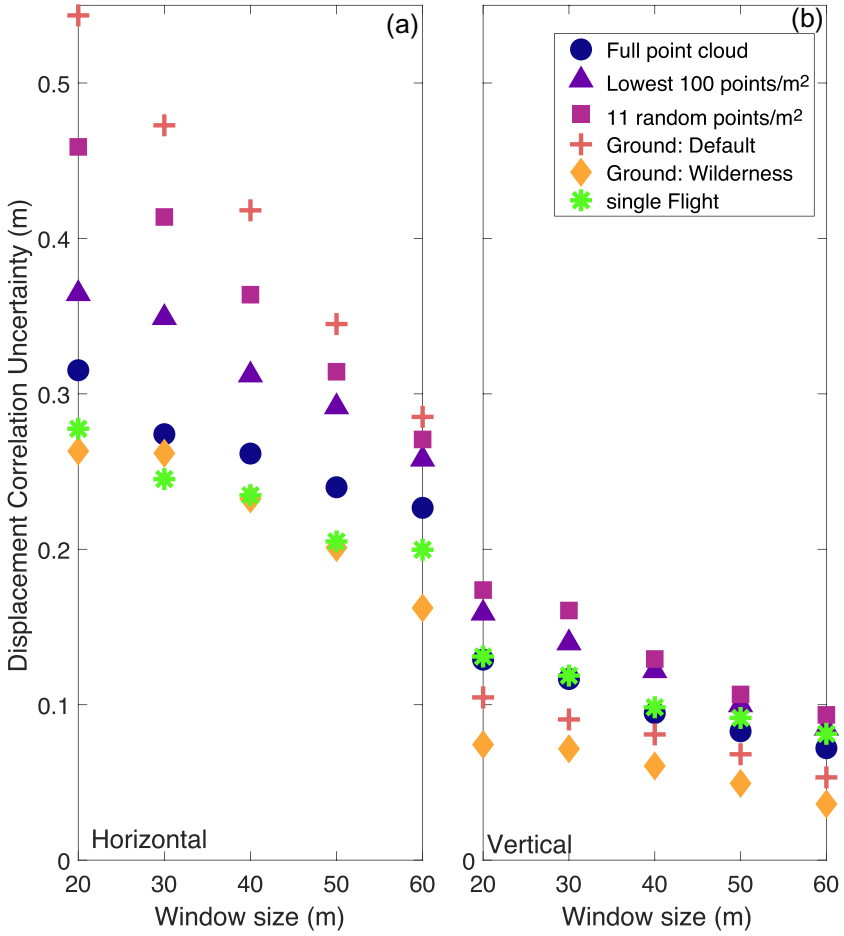

Figure 4. Optimization of the lidar and structure-from-motion point cloud filtering for 3-D differencing. (a) Horizontal correlation uncertainty versus window size. Circle: Full EarthScope lidar and the sUAS data set. Triangle: Full EarthScope data set and the lowest 100 pts/m^2 of the sUAS data set. Square: Full EarthScope data set and a random 10 pts/m^2 from the sUAS data set. Cross: Ground classified points from the EarthScope data set (EarthScope, 2008) and the UAS data set classified with LAStool's lasground_new algorithm using default options (Isenburg, 2019). Diamond: LAStool's wilderness ground classification applied to the lidar and sUAS data sets. Star: EarthScope's Flight 3 that straddles the San Andreas Fault and the full sUAS data set. (b) Vertical correlation uncertainty versus window size. Colors are identical to (a). We prefer the wilderness ground classification due to the low uncertainty and high spatial coverage.

To determine a workflow that minimizes the 3-D displacement uncertainty, we tested several pre-processing approaches (Figure 4). We thinned the 2017 sUAS data to the lowest 100 pts/m^2. We also randomly thinned the 2017 sUAS data so that both data sets have similar point density. This is unlikely to have introduced bias by selecting only ground points, for example. We tested two ground classifications to remove vegetation. The "default ground classification" in Figure 4 represents the ground-classified points available from OpenTopography for the 2007 data and the LAStools default classification applied to the 2017 data (Isenburg, 2019). For the "wilderness ground classification", we applied the wilderness settings in las-ground_new from LAStools to both data sets to remove vegetation with length greater than 3 m. Other commonly applied ground classification approaches remove larger scale features and classify more points as ground. The wilderness option likely worked best at Dry Lake Valley due to the relatively low-to-the-ground and sparse vegetation. The wilderness ground-classified points have 4.1 and 179 pts/m^2 in the lidar and sUAS data sets, respectively, as shown in Figure S3. We performed differencing using only the EarthScope flight line that crosses the San Andreas Fault to minimize the impact of flight line error. We examined each filtering approach using 20- to 60-m window sizes with a 25-m moving window.

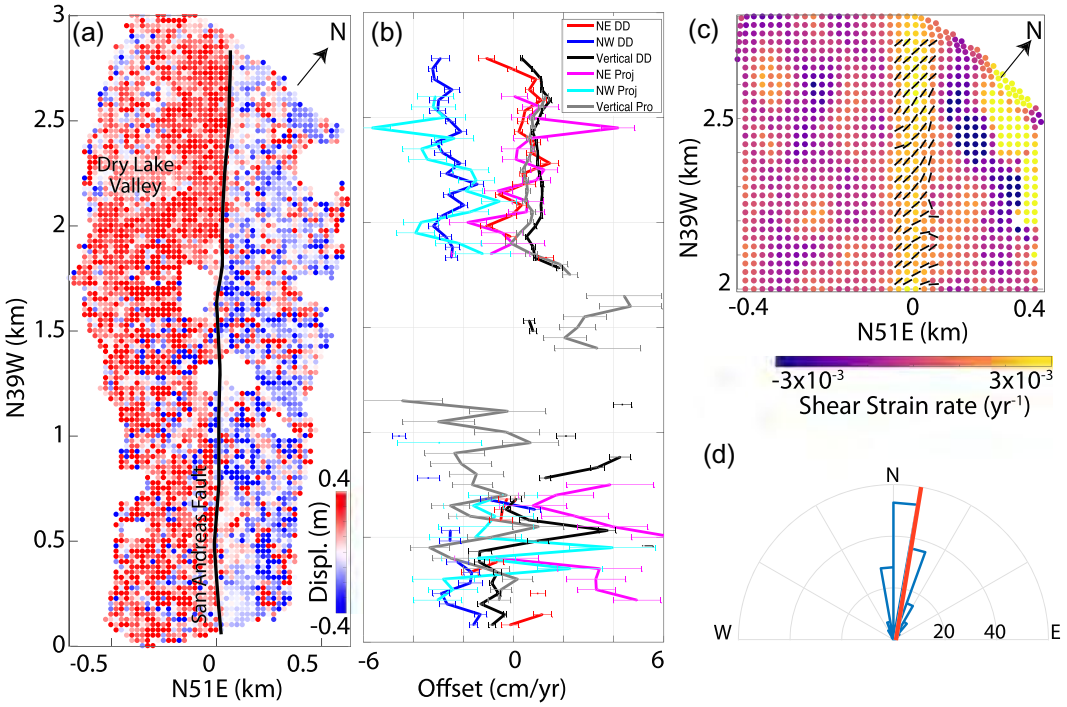

Figure 5. Fault offset and strain derived from the topographic differencing of the 2007 EarthScope Northern California airborne lidar and the 2017 sUAS SfM topography. (a) NW (right-lateral) ICP displacement field plotted for points with horizontal uncertainty less than 1.5 m. The black line is the San Andreas Fault. The coordinate system in (a–c) is aligned with the San Andreas Fault. (b) San Andreas Fault offset rate estimated from the differential discontinuity —red: NE (fault-normal), blue: NW (right-lateral), and black (vertical). Offset rate estimated from the rate projection —pink: NE, light blue: NW, and gray (vertical). (c) Right-lateral shear strain rate. Black lines are the maximum horizontal shortening direction. This shows only the northwestern third of the site where the scatter in the data is lower. (d) Rose diagram shows the maximum horizontal shortening direction from 160 strain tensors. Mean orientation is 9.35° ± 2.6°, which is 48° from the local fault trend.

We assessed the effectiveness of the filtering and window size optimization for improving the displacement results using the displacement correlation uncertainty (Scott et al., 2018), which estimates the uncertainty for each displacement from the scatter in the 24 surrounding displacements over a 100 × 100 m^2 window (Figure S4). The uncertainty is primarily sensitive to noise and landscape characteristics that make a precise alignment challenging and less sensitive to spatially correlated noise like GNSS errors. The unfiltered point clouds produced median horizontal and vertical displacement uncertainty of 22–32 cm and 10–13 cm, respectively. Uncertainty reduced to 16–28 cm (horizontal) and 4–8 cm (vertical) with LAStool's wilderness ground classification. The single flight line and the wilderness ground points have similar horizontal uncertainty, suggesting that flight line offset and differences in how vegetation is sensed in the unfiltered data set contribute a similar uncertainty. Expectedly, displacement correlation uncertainty increased with decreasing window size. Ultimately, we preferred a 40-m size window and the wilderness ground classification due to the low uncertainty and high spatial coverage. The displacement field is shown in Figures 5a and S5.

3.2.3. Fault Slip Rate From the Displacement Discontinuity

We calculated moving averages of 3-D fault offset by differencing ICP displacements across the fault following Scott et al. (2018), as shown in Figure S4. The moving box used for the averaging is 40 × 60 m^2 in the fault-parallel and perpendicular directions, respectively, with the near-fault side lying 60 m from the fault. We averaged the displacements with an inverse weighting of the displacement correlation uncertainty. Let d_{SW} and d_{NE} represent the weighted average of the 3-D vector displacement to the fault's southwest and northeast, respectively. The uncertainty in the average displacements (Δd_{SW} and Δd_{NE}) is the standard error of the weighted mean. The fault-normal, right-lateral, and vertical displacement discontinuity (dd) is the vector subtraction across the fault,

$$dd = d_{sw} - d_{NE}. \quad (1)$$

Because our coordinate system aligns with the San Andreas Fault, we extracted the fault-normal, right-lateral, and vertical displacement discontinuity from the three components of dd. The displacement discontinuity uncertainty (Δdd) is calculated from a propagation of uncertainty,

$$\Delta \mathrm{dd} = \sqrt{\Delta {d_{sw}}^2 + \Delta {d_{NE}}^2}. \quad (2)$$

To calculate rates, we divided the displacement by the time between the acquisitions. The offset rates are shown in Figure 5b, and the average right-lateral slip rate at Dry Lake Valley is 2.5 ± 0.2 cm/yr.

3.2.4. Fault Slip Rate From the Displacement Projection

We solved for the best-fit line to the displacement ($disp$) versus fault-normal distance (x) on both sides of the fault along 40-m wide transects (slope: m, y-intercept: b). We used a linear least-squares inversion weighted by the inverse of the displacement uncertainty. On the south-west side of the fault,

$$disp_{sw} = m_{sw}x + b_{sw}. \quad (3)$$

On the northeast side of the fault,

$$disp_{ne} = m_{ne}x + b_{ne}. \quad (4)$$

We performed a coordinate transformation to place the origin at the fault based on our geomorphic mapping ($x_{fault} = 0$). The offset is the difference in $disp_{sw}$ and $disp_{ne}$ at the fault:

$$offset = disp_{sw} - disp_{ne} = b_{sw} - b_{ne}. \quad (5)$$

We solved for the uncertainty in the offset ($\Delta offset$) using a propagation of uncertainty:

$$\Delta offset = \sqrt{(m_{sw} - m_{ne})^2 \Delta Fx^2 + (\Delta b_{sw})^2 + (\Delta b_{ne})^2}. \quad (6)$$

We assumed a 5-m uncertainty in fault location (ΔFx), although we often know the fault location with greater accuracy. We calculated the covariance in the line-fitting parameters (Equation 6; Δb_{sw} and Δb_{ne}) from the displacement uncertainty. Example transects are shown in Figure S13. The average right-lateral offset rate using this method in Dry Lake Valley is 2.7 ± 0.8 cm/yr.

3.2.5. Horizontal Strain

We calculated strain rate to constrain the fault zone width and to compare differencing results to the surface fractures. We approximated strain as infinitesimal and solved for the 2-D horizontal strain field ($\boldsymbol{e}_{ij}$) using a least-squares inversion of sets of 49 horizontal displacements over 150 × 150 m^2 moving windows (Figure 5c), following Allmendinger et al. (2009) and Scott et al. (2018). Because the coordinate system is aligned with the San Andreas Fault (N39W axis), shear strain reflects fault-parallel right-lateral simple shear. We solved for the principal strain orientation from an eigenvector decomposition of the strain tensor.

3.3. Near-Field Deformation: Surface Fractures

Surface fractures at Dry Lake Valley are our smallest scale of deformation, and we compare their opening to the topographic differencing results. We produced an orthomosaic of fractures along the fault trace with SfM processing of 606 photographs taken with hand-held Nikon D90 and Fuji FinePix cameras on 20 September 2014 (Figure 6). The ~50 × 5 m^2 orthomosaic was georeferenced using ground control points measured with rapid-static GNSS. We did not observe tectonic ground fractures in the 2011 and 2012 summers when conducting paleoseismic studies or in October 2017 when collecting the sUAS data set (Bunds et al., 2020).

We mapped 119 fractures along the fault trace that occur in a left-stepping en echelon pattern and form left-stepping groups that we interpret as R-shears (Figure 6). On average, the surface fractures are 54 cm long, have a maximum width of 1.8 cm, and overlap with adjacent fractures by a factor of 2.2 (i.e., lines drawn along the maximum extension direction cross on average 2.2 fractures). In the field and

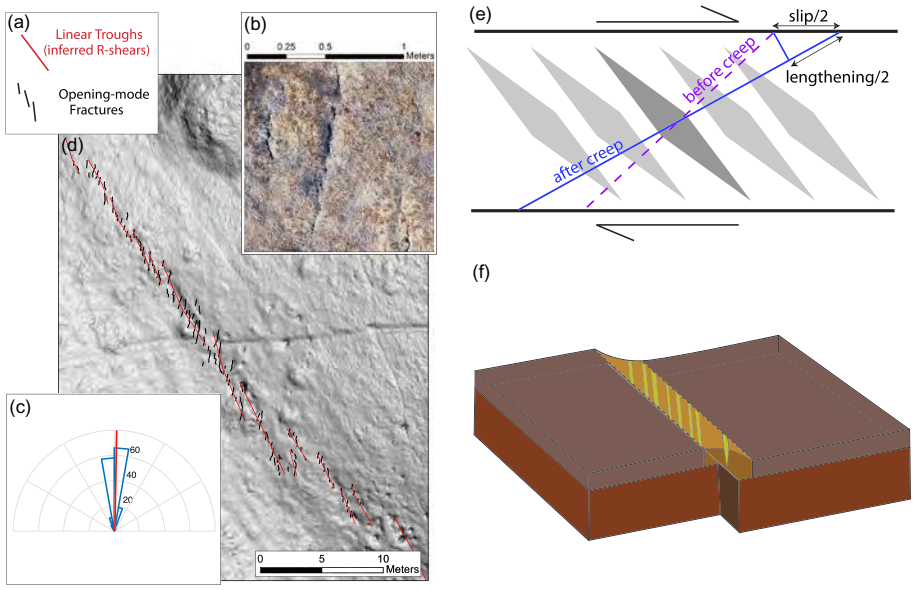

Figure 6. Surface fractures during the 2014 drought. (a) Relationship and (b) field photo of R-shears and extensional fractures. (c) Rose diagram of extensional fractures with a 1.2° ± 1.3° average orientation, ~40° from the local San Andreas Fault trend. (d) Interpreted topographic hillshade, showing fractures (black) and R-shears (red). Figure S13 is the non-interpreted image. (e) Quantifying the relationship between fracture opening and right-lateral fault slip. (f) Our interpretation of creep along the San Andreas Fault: Fractures open at the surface and connect to a narrow fault within 1–3 m below the ground surface (Toke & Arrowsmith, 2015).

orthomosaic imagery, the fractures appear vertical, and the paleoseismic investigation confirmed a subvertical to vertical dip of older, filled subterranean fractures (Toke & Arrowsmith, 2015). The fractures trend 184° on average, forming a 40° angle to the local trend of the San Andreas Fault. We saw no evidence of rotation or shearing along the fractures and interpreted the fractures as Mode 1. We presume that the fractures are entirely tectonic (i.e., not desiccation cracks). Likely, the fractures have a similar depth to their length. Our topographic differencing strain analysis showed that the fault-parallel dilation is 1–2 orders of magnitude smaller than the shear strain, validating this interpretation (Figure S12). We calculated right-lateral slip along the San Andreas from the measured fracture opening of an individual fracture (Figure 6e),

$$Maximum\ slip\ from\ fracture = \frac{\text{Maximum fracture opening}}{\sin(\theta)}, \tag{7}$$

where θ is the angle between fracture orientation and the San Andreas Fault. We corrected for fracture tapering to account for our measurements at the maximum width. We modeled the fractures as trapezoids where each fracture's average width is half its maximum width, giving a fracture tapering correction (Tf) of 0.5,

$$Average\ fault\ slip = T_f \times (Maximum\ slip\ from\ fracture) \times overlap. \tag{8}$$

We considered this to be a minimum opening. Had we assumed ellipsoidal fractures (e.g., Spence & Turcotte, 1985) with average widths greater than half the maximum width, the average opening would be 60% larger. Based on the values above, the average right-lateral fault slip accommodated by Mode 1 fractures is $3.05^{+1.1}_{-0.8}$ cm. The uncertainty reflects differences in repeated measurement of fracture openings. There is additional evidence for fractures: Our 2014 sUAS imagery shows fractures south of where we acquired the hand-held imagery and similar fractures have been observed elsewhere along the creeping fault (e.g., the DeRose Winery, Toke & Arrowsmith, 2015).

Assessing the time over which the fractures formed and accommodated strain is challenging due to the time between field inspections and uncertainty in the amount and timing of the rainfall at Dry Lake Valley. The

fractures formed after the clay-rich soil at the site dried and hardened following the last significant rainfall at the start of the California drought which began in the 2013 water year and extended through the 2014 water year (i.e., October 2012–September 2014: Swain et al., 2014). No fractures were seen in June 2013, although it is possible incipient fractures were unnoticed (Toke & Arrowsmith, 2015).

Based on meteorological data from the USGS Hernandez HDZ rain gauge (California Department of Water Resources, 2020), we place additional bounds on when the fractures mostly likely developed. The Hernandez Station is located 200 m higher in elevation and 20-km SSE from Dry Lake Valley and therefore may have had more rainfall than Dry Lake Valley. The station recorded 44% of the normal rain fall during the drought from November 2012 to February 2014. The 2013 wet season (October 2012–April 2013) was much less wet than typical, but there were two heavy rain events (more than 2-cm rainfall) in November and December. From January to mid-April 2013 measurable rainfall occurred at least every 2 weeks, but the last rainfall event of more than 0.5 cm in 24 h occurred on 8 March 2013. Based on this rainfall record and the fact that we did not observe fractures in June 2013, we infer that the earliest the fractures could have begun to form was mid-April 2013. There were then several months-long dry periods and no significant rain events until late winter 2014. In late February and April 2014, there were rainfall events with 2.5 and 1.7 cm. At the Hernandez gauge, there was no rain between April and when we measured the fractures in September 2014. The shortest period for fracture formation is April to September 2014 (~5 months bounding a single dry season), and we consider this improbable. More likely, the fractures began forming in mid-April 2013 and recorded 1.41 ± 0.08 yr (i.e., 17-months with 1 month uncertainty at the 1σ level) of fault activity before September 2014. Accounting for the uncertainty in opening and time, the opening-mode fractures accommodated $2.2^{+0.8}_{-0.6}$ cm/yr of right-lateral fault slip rate.

4. Results and Discussion

4.1. Deformation Rates

Because of the short spatial and temporal interferometric baselines used for InSAR time-series analysis, the 2016–2020 InSAR velocity map remains coherently adjacent to the fault (Figure 3). Importantly, zooming in to Dry Lake Valley (Figure 3b) shows that deformation is narrowly localized to the San Andreas Fault with strong contrasts in the LOS displacement rate (blue and yellow) on either side of a narrow fault trace (white). Other signals include atmospheric noise in the central valley and in the coastal ranges. The approximate oval shape of subsidence to the southeast of Dry Lake Valley represents the Coalinga Oil Fields.

Because the largest earthquake near Dry Lake Valley during the study period was a M5.3 event in October 2012 at a 9-km depth 30 km to the southeast of the site (USGS: Earthquake Hazards Program, 2012), we conclude that topographic differencing (Figure 5) captures San Andreas Fault creep. At Dry Lake Valley, the sharp change in displacement across the fault suggests that the majority of deformation within 500 m of the fault is accommodated over less than 40 m, the differencing resolution. Right-lateral creep rates are 2.5 ± 0.2 cm/yr and 2.7 ± 0.8 cm/yr calculated from the displacement discontinuity method and displacement-projection methods, respectively (Figure 7). The slip-projection method uncertainty is higher, because flight line offsets near the data set boundary impact the best-fit lines and therefore also the inferred fault offset. The method's slightly greater rate likely reflects error, but we cannot completely rule out that the difference may reflect the greater aperture of the displacement-projection method. Southeast of Dry Lake Valley, displacements are considerably noisier (Figure 5), reflecting the higher vegetation and greater topographic relief where erosional processes are likely more active. Visually, creep is still concentrated along the fault trace. The NE–SW displacement is often negligible, showing only insignificant fault-normal motion. The vertical deformation largely reflects vegetation changes whose signal is pronounced because the hybrid sensors have varying sensitivity to vegetation.

The highest horizontal shear strain rates (Figure 5c) of ~3×10^{-4}/yr occur over an ~100-m aperture that straddles the San Andreas Fault. We use a 150-m window size in the strain calculation, further suggesting that surface creep is localized to no more than several tens of meters from the fault. The instantaneous direction of maximum shortening (Figure 5D) is 9.4° ± 2.1°, which is 47° from the trend of the San Andreas Fault (321°). This result is consistent with the 3° ± 7° average trend of opening mode fractures measured from the orthomosaic imagery. The fault parallel dilation is negligible ($8.5 \times 10^{-6} \pm 5 \times 10^{-5}$/yr).

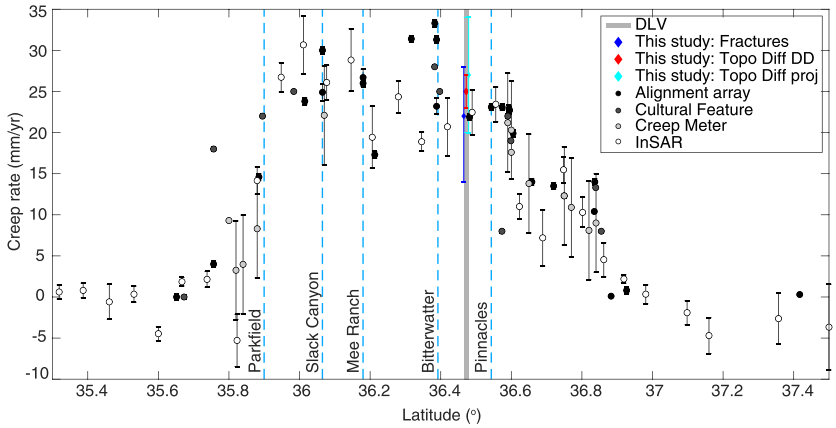

Figure 7. Creep rates from this study (diamonds) and others compiled from the literature based on alignment arrays (Burford & Harsh, 1980; Galehouse & Lienkaemper, 2003; Titus et al., 2006), cultural features (Brown & Wallace, 1968; Burford & Harsh, 1980; Roth & Wallace, 1967), creep meters (Burford, 1988), and InSAR (Tong et al., 2013) measurements. Our three measurements (diamonds) are all at Dry Lake Valley (gray line) and are separated for visual clarity only. Topo diff: Topographic difference rate from the displacement discontinuity (*dd*) and the displacement-projection (proj) methods.

4.2. Comparison of Fault Creep Rates at Different Apertures

Over a 3- to 4-m aperture, the opening-mode fractures accommodate 90% ± 30% of the topographic differencing creep rate. Especially given the assumption of trapezoidal fractures which may underestimate the opening, the fractures are likely to accommodate the full topographic differencing rate. If the differencing rate is larger than the fracture rate, the remaining strain is likely accommodated at most several tens of meters from the fault as distributed deformation.

At Dry Lake Valley, the slip rate inferred from a 110-m long alignment array measured from 1967 to 1974 is 2.19 ± 0.04 cm/yr (Burford & Harsh, 1980) and a 2006–2010 InSAR time series is 2.24 ± 0.27 cm/yr (Tong et al., 2013). The alignment array rate is almost within uncertainty of the 2.5 ± 0.2 cm/yr topographic differencing rate, and thus, we conclude that the difference likely reflects error. However, we cannot exclude either a long-term rate change or that month to year-long episodic creep events are responsible. Tong et al.'s (2013) InSAR rate is within the uncertainty of our displacement discontinuity rate. We conclude that the topographic differencing rates are consistent with other data sets given the uncertainty.

4.3. Fracturing Within the Fault Zone

Riedel shears, extensional fractures, and short discontinuous faults with a few centimeters of offset are typically the main surface expression in moderate magnitude earthquakes, such as the 2004 M6.0 Parkfield earthquake (e.g., Rymer et al., 2006) and the 2014 M6.0 Napa, CA, earthquake (e.g., Brooks et al., 2017). In larger strike-slip earthquakes, Riedel shear fractures also form, particularly along less mature faults (Lin & Nishikawa, 2011; Quigley et al., 2012). Opening mode fractures can form as part of a Riedel system or independently. Off-fault fractures can form due to dynamic stresses from propagating seismic waves which can also cause sand and clasts to fall and prop fractures open (Loveless et al., 2005; Scott et al., 2016).

We infer that the fractures formed along the fault zone at Dry Lake Valley are due to progressive fault slip, fracture formation, and opening, like the factures formed in moderate magnitude earthquakes. Portions of the fractures may be associated with preexisting desiccation cracks, but their pervasive nature through the fault zone, optimal alignment, and straight-line lengths (which exceed that of polygonal cracking at Dry Lake Valley) suggest that they are primarily unassociated with desiccation cracking. The clayey soil remained stiff in the absence of rain, and the fractures were progressively opened by ongoing creep. Over ~17 months, the site did not receive enough rain to saturate the soil and close the fractures and/or inhibit fracture formation (Toke & Arrowsmith, 2015). The nearby M5.3 earthquake in October 2012 (USGS:

Earthquake Hazards Program, 2012) is unlikely to have caused enough shaking or surface deformation at Dry Lake Valley to open the cracks and cause debris to continue to prop them open.

Fracture opening may be modulated by accelerated creep events (Khoshmanesh & Shirzaei, 2018b; Wei et al., 2013) along Central San Andreas Fault that increase moment release relative to background and typically last for 2 months to 2 yr. However, to the best of our knowledge, no studies measured creep events during the timeframe of the fracture opening, at least in part due to the low number of SAR satellites in orbit at that time. Therefore, we do not know if the opening of the surface fractures was modulated by a creep event. The slip localization to within 5 m of the fault trace implies that slip likely becomes localized to a discrete fault plane very near the surface. The shift to en echelon fractures instead of a discrete fault plane may reflect plastic yielding ahead of the upward propagating energy as the rock strength decreases towards the surface (Brooks et al., 2017).

4.4. Off-Fault Deformation

Along mature faults (>85 km of offset), 85%–95% of the deformation is accommodated along the main fault trace and not along secondary faults or as distributed deformation (Dolan & Haravitch, 2014). The San Andreas Fault has over 315 km of offset and therefore is considered mature (Mathews, 1976). Still, the deformation along creeping segments varies from being highly localized (meters-wide) to distributed over 1–2 km, particularly near releasing bends (DeLong et al., 2010; Lindsey et al., 2014). Lindsey et al. (2014) attribute distributed deformation along releasing bends to lower normal stresses that promote distributed yielding and microcracking.

Comparing fractures to topographic differencing slip rate results suggests that 90% ± 30% of the 1-km aperture deformation is accommodated over 3–4 m. The topographic differencing and InSAR rate fields show no strong evidence of off-fault deformation, suggesting that any deformation not taken up by the fractures is accommodated within at most a few tens of meters of the fault. The orientation of the opening mode fractures and the maximum shortening oriented ~45° from the San Andreas Fault suggests that the fault is well-oriented for strike-slip faulting. Dry Lake Valley is surrounded by an ~1-km wide surface alluvium deposit (Jennings & Strand, 1958), which likely contributes to the shallow fracturing yet does not result in the broad deformation often observed for coseismic ruptures in soft sediments (Teran et al., 2015; Zinke et al., 2014). We propose that the slip localization at Dry Lake Valley results from the San Andreas Fault being mature and its near perfect alignment for regional tectonic slip. Improved constraints on deformation rates along the releasing bend immediately to Dry Lake Valley's southeast would reveal how a minor geometric complexity impacts distributed deformation.

Other authors report aperture-dependent deformation rates along the central San Andreas Fault. Near-field (10-m aperture) creep rates are 20% lower than intermediate-field (10 m to 1 km) rates at Mee Ranch (Figure 1; Titus et al., 2006). Deformation is distributed along a releasing bend at Mustang Ridge where the fault outcrops in Franciscan sandstone, chert, and conglomerate (DeLong et al., 2010). Like in an earthquake, distributed deformation along the creeping fault varies and geometric complexity. Ultimately, knowledge of the variability of strain localization has implications for slip rate, moment accumulation, and hazard.

5. Conclusions

We measured deformation and slip localization at three spatial scales, from near- to far-field, at the Dry Lake Valley paleoseismic field site along the creeping portion of the central San Andreas Fault from InSAR, topographic differencing, and surface fractures. Performing differencing with lidar and SfM-derived point clouds presents a unique challenge due to the varying sensitivity to vegetation and point density of the data sets. The topographic differencing method constrains spatially dense rates at an aperture intermediate to near-field creepmeters and alignment arrays and far-field InSAR and GNSS data sets. Using topographic differencing, we resolved a creep rate of 2.5 ± 0.2 cm/yr, which is consistent with other geodetic rates. A 90% ± 30% of the deformation measured at a 1-km aperture was accommodated across a fault zone less than 5 m wide along a short reach of the Dry Lake Valley site. The high localization reflects the well-oriented fault and the fault's structural maturity and is consistent with expectations of an earthquake along a mature fault.

Data Availability Statement

The 2007 lidar (https://doi.org/10.5069/G9057CV2) and 2017 sUAS (https://doi.org/10.5069/G91N7Z92) data sets are available from OpenTopography (www.opentopography.org). The Sentinel-1 data are available online (https://sentinel.esa.int). Our fracture measurements are included in the supporting information.

Acknowledgments

Scott was supported by the National Science Foundation Postdoctoral Fellowship 1625221, the Southern California Earthquake Center through Award 19123, and by the School of Earth and Space Exploration at Arizona State University. Bunds and Toke are grateful for an Engaged Learning grant and an award from the College of Science Scholarly Activities Committee at Utah Valley University. Toke and Bunds were supported by the Southern California Earthquake Center Awards 12050 and 13147. The National Science Foundation grant EAR-1735630 supported Manoochehr Shirzaei. We thank Utah Valley University students Jeremy Saldivar, Marissa Keck, Logan Woolstenhume, McKenzie Ranney, Serena Smith, and Joseph Phillips for help collecting the sUAS data in 2017. We are grateful for conversations with J. Barrett Salisbury, Ramon Arrowsmith, and other colleagues involved in paleoseismology field work at Dry Lake Valley. We thank Edwin Nissen and an anonymous reviewer for constructive comments during the review process.

References

Allmendinger, R. W., Loveless, J. P., Pritchard, M. E., & Meade, B. (2009). From decades to epochs: Spanning the gap between geodesy and structural geology of active mountain belts. *Journal of Structural Geology*, *31*(11), 1409–1422. https://doi.org/10.1016/j.jsg.2009.08.008

Arrowsmith, R., McNally, K., & Davis, J. (1997). Potential for earthquake rupture and M 7 earthquakes along the Parkfield, Cholame, and Carrizo segments of the San Andreas Fault. *Seismological Research Letters*, *68*(6), 902–916. https://doi.org/10.1785/gssrl.68.6.902

Bakun, W. H. (1999). Seismic activity of the San Francisco Bay region. *Bulletin of the Seismological Society of America*, *89*(3), 764–784.

Barnhart, W. D., Gold, R. D., Shea, H. N., Peterson, K. E., Briggs, R. W., & Harbor, D. J. (2019). Vertical coseismic offsets derived from high-resolution stereogrammetric DSM differencing: The 2013 Baluchistan, Pakistan earthquake. *Journal of Geophysical Research: Solid Earth*, *124*, 6039–6055. https://doi.org/10.1029/2018JB017107

Besl, P. J., & McKay, N. D. (1992). A method for registration of 3-D shapes. *IEEE Transactions on Pattern Analysis and Machine Intelligence*, *14*(2), 239–256. https://doi.org/10.1109/34.121791

Brooks, B. A., Minson, S. E., Glennie, C. L., Nevitt, J. M., Dawson, T., Rubin, R., et al. (2017). Buried shallow fault slip from the South Napa earthquake revealed by near-field geodesy. *Science Advances*, *3*, e1700525. https://doi.org/10.1126/sciadv.1700525

Brown, R. D., & Wallace, R. E. (1968). Current and historic fault movement along the San Andreas Fault between Paicines and Camp Dix, California. In A. Grantz & W. R. Dickinson (Eds.), *Proceedings, conference on geologic problems of the San Andreas Fault system* (Vol. 11, pp. 22–39). California: Stanford University Publications in Geological Sciences.

Bunds, M., Scott, C. P., Toke, N. A., Saldivar, J., Woolstenhulme, L., Phillps, J., et al. (2020). High resolution topography of the Central San Andreas Fault at Dry Lake Valley, California, USA. OpenTopography. https://doi.org/10.5069/G91N7Z92

Burford, R. O. (1988). Retardations in fault creep rates before local moderate earthquakes along the San Andreas fault system, Central California. *Pure and Applied Geophysics PAGEOPH*, *126*(2–4), 499–529. https://doi.org/10.1007/BF00879008

Burford, R. O., & Harsh, P. W. (1980). Slip on the San Andreas fault in Central California from alinement array surveys. *Bulletin of the Seismological Society of America*, *4*, 1233–1261.

Burgmann, R., Schmidt, D., Nadeau, R. M., D'Alessio, M. A., Fielding, E. J., Manaker, D., et al. (2000). Earthquake potential along the northern Hayward Fault, California. *Science*, *289*(5482), 1178–1182. https://doi.org/10.1126/science.289.5482.1178

California Department of Water Resources (2020). Hernandez (HDZ) precipitation data. Retrieved from https://cdec.water.ca.gov/dynamicapp/QueryF?s=HDZ

Chen, K. H., & Bürgmann, R. (2017). Creeping faults: Good news, bad news? *Reviews of Geophysics*, *55*, 282–286. https://doi.org/10.1002/2017RG000565

Chen, Y., & Medioni, G. (1992). Object modelling by registration of multiple range images. *Image and Vision Computing*, *10*(3), 145–155. https://doi.org/10.1016/0262-8856(92)90066-C

Constantini, M., & Rosen, P. A. (1999). A generalized phase unwrapping approach for sparse data. *Proceedings of the IEEE 1999 International Geoscience and Remote Sensing Symposium (IGARSS)*.

Costantini, M. (1998). A novel phase unwrapping method based on network programming. *IEEE Transactions on Geoscience and Remote Sensing*, *36*(3), 813–821. https://doi.org/10.1109/36.673674

DeLong, S. B., Hilley, G. E., Rymer, M. J., & Prentice, C. (2010). Fault zone structure from topography: Signatures of en echelon fault slip at Mustang Ridge on the San Andreas Fault, Monterey County, California. *Tectonics*, *29*, TC5003. https://doi.org/10.1029/2010TC002673

DeMets, C., Gordon, R. G., Argus, D. F., & Stein, S. (1994). Effect of recent revisions to the geomagnetic reversal time scale on estimates of current plate motions. *Geophysical Research Letters*, *21*(20), 2191–2194. https://doi.org/10.1029/94GL02118

Dolan, J. F., & Haravitch, B. D. (2014). How well do surface slip measurements track slip at depth in large strike-slip earthquakes? The importance of fault structural maturity in controlling on-fault slip versus off-fault surface deformation. *Earth and Planetary Science Letters*, *388*, 38–47. https://doi.org/10.1016/j.epsl.2013.11.043

EarthScope (2008). EarthScope northern California LiDAR project. NSF OpenTopography Facility. https://doi.org/10.5069/G9057CV2

ESA (2020). Sentinel-1 Pod products performance. Retrieved from https://sentinel.esa.int/documents/247904/3455957/Sentinel-1-POD-Products-Performance.pdf

Farr, T. G., Rosen, P. A., Caro, E., Crippen, R., Duren, R., Hensley, S., et al. (2007). The shuttle radar topography mission. *Reviews of Geophysics*, *45*, RG2004. https://doi.org/10.1029/2005RG000183

Franceschetti, G., & Lanari, R. (1999). *Synthetic Aperture Radar Processing*. New York: CRC Press.

Galehouse, J. J., & Lienkaemper, J. J. (2003). Inferences drawn from two decades of alinement array measurements of creep on faults in the San Francisco Bay region. *Bulletin of the Seismological Society of America*, *93*(6), 2415–2433. https://doi.org/10.1785/0120020226

Gao, J., Sultan, H., Hu, J., & Tung, W.-W. (2010). Denoising nonlinear time series by adaptive filtering and wavelet shrinkage: A comparison. *IEEE Signal Processing Letters*, *17*(3), 237–240. https://doi.org/10.1109/LSP.2009.2037773

Geiger, A., Lenz, P., & Urtasun, R. (2012). Are we ready for autonomous driving? The KITTI vision benchmark suite. In *2012 IEEE conference on computer vision and pattern recognition* (pp. 3354–3361). Providence, RI: IEEE.

Hanssen, R. (2001). *Radar Interferometry: Data Interpretation and Error Analysis* (Vol. 2). Dordrecht: Kluwer Academic Press. https://doi.org/10.1007/0-306-47633-9

Harris, R. A. (2017). Large earthquakes and creeping faults: Large earthquakes and creeping faults. *Reviews of Geophysics*, *55*, 169–198. https://doi.org/10.1002/2016RG000539

Howell, A., Nissen, E., Stahl, T., Clark, K., Kearse, J., van Dissen, R., et al. (2020). Three-Dimensional surface displacements during the 2016 M_W 7.8 Kaikōura Earthquake (New Zealand) from photogrammetry-derived point clouds. *Journal of Geophysical Research: Solid Earth*, *125*, e2019JB018739. https://doi.org/10.1029/2019JB018739

Isenburg, M. (2019). LAStools - Efficient tools for lidar processing. Retrieved from www.lastools.org

Jennings, C. W., & Strand, R. G. (1958). Geologic map of California: Santa Cruz sheet. State of California: Department of Natural Resources.

Johnson, K., Nissen, E., Saripalli, S., Arrowsmith, J. R., McGarey, P., Scharer, K., et al. (2014). Rapid mapping of ultrafine fault zone topography with structure from motion. *Geosphere*, *10*(5), 969–986. https://doi.org/10.1130/GES01017.1

Johnson, K. M. (2013). Is stress accumulating on the creeping section of the San Andreas fault? *Geophysical Research Letters*, *40*, 6101–6105. https://doi.org/10.1002/2013GL058184

Johnson, S. Y., Watt, J. T., Hartwell, S. R., & Kluesner, J. W. (2018). Neotectonics of the Big Sur Bend, San Gregorio–Hosgri fault system, Central California. *Tectonics*, *37*, 1930–1954. https://doi.org/10.1029/2017TC004724

Jolivet, R., Simons, M., Agram, P. S., Duputel, Z., & Shen, Z.-K. (2015). Aseismic slip and seismogenic coupling along the Central San Andreas Fault. *Geophysical Research Letters*, *42*, 297–306. https://doi.org/10.1002/2014GL062222

Khoshmanesh, M., & Shirzaei, M. (2018a). Episodic creep events on the San Andreas Fault caused by pore pressure variations. *Nature Geoscience*, *11*(8), 610–614. https://doi.org/10.1038/s41561-018-0160-2

Khoshmanesh, M., & Shirzaei, M. (2018b). Multiscale dynamics of aseismic slip on Central San Andreas Fault. *Geophysical Research Letters*, *45*, 2274–2282. https://doi.org/10.1002/2018GL077017

Langenheim, V. E., Jachens, R. C., Graymer, R. W., Colgan, J. P., Wentworth, C. M., & Stanley, R. G. (2013). Fault geometry and cumulative offsets in the central coast ranges, California: Evidence for northward increasing slip along the San Gregorio–San Simeon–Hosgri fault. *Lithosphere*, *5*(1), 29–48. https://doi.org/10.1130/L233.1

Lin, A., & Nishikawa, M. (2011). Riedel shear structures in the co-seismic surface rupture zone produced by the 2001 M_w 7.8 Kunlun earthquake, northern Tibetan Plateau. *Journal of Structural Geology*, *33*(9), 1302–1311. https://doi.org/10.1016/j.jsg.2011.07.003

Lindsey, E. O., Fialko, Y., Bock, Y., Sandwell, D. T., & Bilham, R. (2014). Localized and distributed creep along the southern San Andreas Fault. *Journal of Geophysical Research: Solid Earth*, *119*, 7909–7922. https://doi.org/10.1002/2014JB011275

Lisowski, M., & Prescott, W. (1981). Short-range distance measurements along the San Andreas fault system in Central California, 1975 to 1979. *Bulletin of the Seismological Society of America*, *71*, 1607–1624.

Loveless, J. P., Hoke, G. D., Allmendinger, R. W., González, G., Isacks, B. L., & Carrizo, D. A. (2005). Pervasive cracking of the northern Chilean Coastal Cordillera: New evidence for forearc extension. *Geology*, *33*(12), 973. https://doi.org/10.1130/G22004.1

Lowe, D. (2004). Distinctive image features from scale-invariant keypoints. *International Journal of Com- Puter Vision*, *60*(2), 91–110. https://doi.org/10.1023/B:VISI.0000029664.99615.94

Mathews, V. (1976). Correlation of Pinnacles and Neenach volcanic formations and their bearing on San Andreas fault problem. *Bulletin of the American Association of Petroleum Geologists*, *60*, 2128–2141.

Milliner, C. W. D., Dolan, J. F., Hollingsworth, J., Leprince, S., & Ayoub, F. (2016). Comparison of coseismic near-field and off-fault surface deformation patterns of the 1992 M_w 7.3 Landers and 1999 M_w 7.1 Hector Mine earthquakes: Implications for controls on the distribution of surface strain. *Geophysical Research Letters*, *43*, 10,115–10,124. https://doi.org/10.1002/2016GL069841

Murray, J., & Langbein, J. (2006). Slip on the San Andreas Fault at Parkfield, California, over two earthquake cycles, and the implications for seismic hazard. *Bulletin of the Seismological Society of America*, *96*(4B), S283–S303. https://doi.org/10.1785/0120050820

Nissen, E., Krishnan, A. K., Arrowsmith, J. R., & Saripalli, S. (2012). Three-dimensional surface displacements and rotations from differencing pre- and post-earthquake LiDAR point clouds. *Geophysical Research Letters*, *39*, L16301. https://doi.org/10.1029/2012GL052460

Nissen, E., Maruyama, T., Ramon Arrowsmith, J., Elliott, J. R., Krishnan, A. K., Oskin, M. E., & Saripalli, S. (2014). Coseismic fault zone deformation revealed with differential lidar: Examples from Japanese M_w∼7 intraplate earthquakes. *Earth and Planetary Science Letters*, *405*, 244–256. https://doi.org/10.1016/j.epsl.2014.08.031

Oppenheimer, D. H., Bakun, W. H., Parsons, T., Simpson, R. W., Boatwright, J., & Uhrhammer, R. A. (2010). The 2007 *M* 5.4 Alum Rock, California, earthquake: Implications for future earthquakes on the central and southern Calaveras Fault. *Journal of Geophysical Research*, *115*, B08305. https://doi.org/10.1029/2009JB006683

Pearson, C., & Snay, R. (2013). Introducing HTDP 3.1 to transform coordinates across time and spatial reference frames. *GPS Solutions*, *17*(1), 1–15. https://doi.org/10.1007/s10291-012-0255-y

Prentice, C. S., Crosby, C. J., Whitehill, C. S., Arrowsmith, J. R., Furlong, K. P., & Phillips, D. A. (2009). Illuminating northern California's active faults. *Eos, Transactions American Geophysical Union*, *90*(7), 55–55. https://doi.org/10.1029/2009EO070002

Quigley, M., van Dissen, R., Litchfield, N., Villamor, P., Duffy, B., Barrell, D., et al. (2012). Surface rupture during the 2010 Mw 7.1 Darfield (Canterbury) earthquake: Implications for fault rupture dynamics and seismic-hazard analysis. *Geology*, *40*(1), 55–58. https://doi.org/10.1130/G32528.1

Roth, E. F., & Wallace, R. E. (1967). Rates and patterns of progressive deformation. The Parkfield-Cholame California Earthquakes: U.S. Geological Survey Professional Paper, *579*, 23–40.

Rymer, M. J., Tinsley, J. C., Treiman, J. A., Arrowsmith, J. R., Clahan, K. B., Rosinski, A. M., et al. (2006). Surface fault slip associated with the 2004 Parkfield, California, earthquake. *Bulletin of the Seismological Society of America*, *96*(4B), S11–S27. https://doi.org/10.1785/0120050830

Sansosti, E., Berardino, P., Manunta, M., Serafino, F., & Fornaro, G. (2006). Geometrical SAR image registration. *IEEE Transactions on Geoscience and Remote Sensing*, *44*(10), 2861–2870. https://doi.org/10.1109/TGRS.2006.875787

Scott, C., Champenois, J., Klinger, Y., Nissen, E., Maruyama, T., Chiba, T., & Arrowsmith, R. (2019). 2016 M7 Kumamoto, Japan, earthquake slip field derived from a joint inversion of differential Lidar topography, optical correlation, and InSAR surface displacements. *Geophysical Research Letters*, *46*, 6341–6351. https://doi.org/10.1029/2019GL082202

Scott, C. P., Allmendinger, R. W., González, G., & Loveless, J. P. (2016). Coseismic extension from surface cracks reopened by the 2014 Pisagua, northern Chile, earthquake sequence. *Geology*, *44*(5), 387–390. https://doi.org/10.1130/G37662.1

Scott, C. P., Arrowsmith, J. R., Nissen, E., Lajoie, L., Maruyama, T., & Chiba, T. (2018). The *M* 7 2016 Kumamoto, Japan, earthquake: 3-D deformation along the fault and within the damage zone constrained from differential Lidar topography. *Journal of Geophysical Research: Solid Earth*, *123*, 6138–6155. https://doi.org/10.1029/2018JB015581

Shan, S., Bevis, M., Kendrick, E., Mader, G. L., Raleigh, D., Hudnut, K., et al. (2007). Kinematic GPS solutions for aircraft trajectories: Identifying and minimizing systematic height errors associated with atmospheric propagation delays. *Geophysical Research Letters*, *34*, L23S07. https://doi.org/10.1029/2007GL030889

Shirzaei, M. (2013). A wavelet-based multitemporal DInSAR algorithm for monitoring ground surface motion. *IEEE Geoscience and Remote Sensing Letters*, *10*(3), 456–460. https://doi.org/10.1109/LGRS.2012.2208935

Shirzaei, M., & Bürgmann, R. (2012). Topography correlated atmospheric delay correction in radar interferometry using wavelet transforms. *Geophysical Research Letters*, *39*, L01305. https://doi.org/10.1029/2011GL049971

Shirzaei, M., & Bürgmann, R. (2013). Time-dependent model of creep on the Hayward fault from joint inversion of 18 years of InSAR and surface creep data. *Journal of Geophysical Research: Solid Earth*, *118*, 1733–1746. https://doi.org/10.1002/jgrb.50149

Shirzaei, M., Bürgmann, R., & Fielding, E. J. (2017). Applicability of Sentinel-1 terrain observation by progressive scans multitemporal interferometry for monitoring slow ground motions in the San Francisco Bay Area: Sentinel-1 multitemporal interferometry. *Geophysical Research Letters*, *44*, 2733–2742. https://doi.org/10.1002/2017GL072663

Sieh, K. (1978). Central California foreshocks of the great 1857 earthquake. *Bulletin of the Seismological Society of America*, *68*, 1731–1749.

Snavely, N., Seitz, S. N., & Szeliski, R. (2008). Modeling the world from internet photo collections. *International Journal of Computer Vision*, *80*(2), 189–210. https://doi.org/10.1007/s11263-007-0107-3

Snay, R. (1999). Using the HTDP software to transform spatial coordinates across time and between reference frames. *Surveying and Land Information Systems*, *59*(1), 15–25.

Snay, R. (2003). Horizontal time-dependent positioning. https://www.google.com/calendar?tab=mc1, (November).

Spence, D. A., & Turcotte, D. L. (1985). Magma-driven propagation of cracks. *Journal of Geophysical Research*, *90*(B1), 575–580. https://doi.org/10.1029/JB090iB01p00575

Swain, D. L., Tsiang, M., Haugen, M., Singh, A., Charland, A., Rajaratum, B., & Diffenbaugh, N. S. (2014). The extraordinary California drought of 2013–2014: Character, context, and the role of climate change. [in "Explaining Extremes of 2013 from a Climate Perspective"]. *Bulletin of the American Meteorological Society*, *95*, S3–S7.

Teran, O. J., Fletcher, J. M., Oskin, M. E., Rockwell, T. K., Hudnut, K. W., Spelz, R. M., et al. (2015). Geologic and structural controls on rupture zone fabric: A field-based study of the 2010 Mw 7.2 El Mayor–Cucapah earthquake surface rupture. *Geosphere*, *11*(3), 899–920. https://doi.org/10.1130/GES01078.1

Titus, S. J., DeMets, C., & Tikoff, B. (2006). Thirty-five-year creep rates for the creeping segment of the San Andreas Fault and the effects of the 2004 Parkfield earthquake: Constraints from alignment arrays, continuous global positioning system, and creepmeters. *Bulletin of the Seismological Society of America*, *96*(4B), S250–S268. https://doi.org/10.1785/0120050811

Titus, S. J., Housen, B., & Tikoff, B. (2007). A kinematic model for the Rinconada fault system in Central California based on structural analysis of en echelon folds and paleomagnetism. *Journal of Structural Geology*, *29*(6), 961–982. https://doi.org/10.1016/j.jsg.2007.02.004

Toke, N. A., & Arrowsmith, J. R. (2006). Reassessment of a slip budget along the Parkfield segment of the San Andreas Fault. *Bulletin of the Seismological Society of America*, *96*(4B), S339–S348. https://doi.org/10.1785/0120050829

Toke, N. A., & Arrowsmith, J. R. (2015). Examining the cause of prehistoric ground deformation at the Dry Lake Valley Site along the creeping section of the San Andreas Fault, San Benito, California (Southern California earthquake Center no. 13147).

Tong, X., Sandwell, D. T., & Smith-Konter, B. (2013). High-resolution interseismic velocity data along the San Andreas Fault from GPS and InSAR. *Journal of Geophysical Research: Solid Earth*, *118*, 369–389. https://doi.org/10.1029/2012JB009442

Tong, X., Sandwell, D. T., & Smith-Konter, B. (2015). An integral method to estimate the moment accumulation rate on the creeping section of the San Andreas Fault. *Geophysical Journal International*, *203*(1), 48–62. https://doi.org/10.1093/gji/ggv269

Toppozada, T. R., Branum, D. M., Reichle, M. S., & Hallstrom, C. L. (2002). San Andreas Fault zone, California: M ≥ 5.5 earthquake history. *Bulletin of the Seismological Society of America*, *92*(7), 2555–2601. https://doi.org/10.1785/0120000614

Torrence, C., & Compo, G. P. (1998). A practical guide to wavelet analysis. *Bulletin of the American Meteorological Society*, *79*(1), 61–78. https://doi.org/10.1175/1520-0477(1998)079%3C0061:APGTWA%3E2.0.CO;2

USGS: Earthquake Hazards Program (2012). M 5.3—Central California. Retrieved from https://earthquake.usgs.gov/earthquakes/event-page/nc71863625/executive

Vallage, A., Klinger, Y., Grandin, R., Bhat, H. S., & Pierrot-Deseilligny, M. (2015). Inelastic surface deformation during the 2013 M_w 7.7 Balochistan, Pakistan, earthquake. *Geology*, *43*(12), 1079–1082. https://doi.org/10.1130/G37290.1

Wedmore, L. N. J., Gregory, L. C., McCaffrey, K. J. W., Goodall, H., & Walters, R. J. (2019). Partitioned off-fault deformation in the 2016 Norcia earthquake captured by differential terrestrial laser scanning. *Geophysical Research Letters*, *46*, 3199–3205. https://doi.org/10.1029/2018GL080858

Wei, M., Kaneko, Y., Liu, Y., & McGuire, J. J. (2013). Episodic fault creep events in California controlled by shallow frictional heterogeneity. *Nature Geoscience*, *6*(7), 566–570. https://doi.org/10.1038/ngeo1835

Yague-Martinez, N., Prats-Iraola, P., Rodriguez Gonzalez, F., Brcic, R., Shau, R., Geudtner, D., et al. (2016). Interferometric processing of Sentinel-1 TOPS data. *IEEE Transactions on Geoscience and Remote Sensing*, *54*(4), 2220–2234. https://doi.org/10.1109/TGRS.2015.2497902

Zinke, R., Hollingsworth, J., & Dolan, J. F. (2014). Surface slip and off-fault deformation patterns in the 2013 M_W 7.7 Balochistan, Pakistan earthquake: Implications for controls on the distribution of near-surface coseismic slip. *Geochemistry, Geophysics, Geosystems*, *15*, 5034–5050. https://doi.org/10.1002/2014GC005538